Centrifuge modelling of the progressive failure of geosynthetic-reinforced embankments

G. Zheng[1], B. Xia[2], H. Zhou[3], X. Yu[4], Y. Diao[5] and Y. Du[6]

[1]*School of Civil Engineering, Tianjin University, Tianjin, China; Key Laboratory of Coast Civil Structure Safety, Tianjin University, Ministry of Education, Tianjin, China; State Key Laboratory of Hydraulic Engineering Simulation and Safety, Tianjin University, Tianjin, China, E-mail: zhenggang1967@163.com*
[2]*School of Civil Engineering, Tianjin University, Tianjin, China; Key Laboratory of Coast Civil Structure Safety, Tianjin University, Ministry of Education, Tianjin, China, E-mail: boyang_1027@tju.edu.cn*
[3]*School of Civil Engineering, Tianjin University, Tianjin, China; Key Laboratory of Coast Civil Structure Safety, Tianjin University, Ministry of Education, Tianjin, China; Key Laboratory of Earthquake Engineering Simulation and Seismic Resilience of China Earthquake Administration, Tianjin University, Tianjin, China, E-mail: hzzhou@tju.edu.cn (corresponding author)*
[4]*School of Civil Engineering, Tianjin University, Tianjin, China; Key Laboratory of Coast Civil Structure Safety, Tianjin University, Ministry of Education, Tianjin, China, E-mail: yuxiaoxuan@tju.edu.cn*
[5]*School of Civil Engineering, Tianjin University, Tianjin, China; Key Laboratory of Coast Civil Structure Safety, Tianjin University, Ministry of Education, Tianjin, China; Key Laboratory of Coast Civil Structure Safety, Tianjin University, Ministry of Education, Tianjin, China, E-mail: yudiao@tju.edu.cn*
[6]*School of Civil Engineering, Tianjin University, Tianjin, China; Key Laboratory of Coast Civil Structure Safety, Tianjin University, Ministry of Education, Tianjin, China; Key Laboratory of Coast Civil Structure Safety, Tianjin University, Ministry of Education, Tianjin, China, E-mail: dymtju@tju.edu.cn*

Received 05 April 2023, accepted 17 August 2023, first published online 29 August 2023

ABSTRACT: Understanding the failure mechanism of geosynthetic-reinforced embankments on soft foundations is crucial for ensuring safety in design. This study aimed to investigate the failure mechanism and stability of embankments reinforced with varying layers and lengths of geosynthetic reinforcements utilising centrifuge testing and numerical modelling. The results show that a foundation under construction exhibits a progressive shear failure coupled with a tensile failure of the geosynthetic reinforcement. The plastic shear strain in the soft clay layer initiates at the centreline, shoulder and embankment toe and propagates both forward and backward until a critical slip surface develops. The tensile failure of the geosynthetic was observed at the embankment centre. Comparatively, implementing two shorter layers of geosynthetics proved more advantageous for overall stability than using a single layer with the entire length. By analysing the strain distribution in the foundation, the deformation modes of the embankment reinforced by different numbers of geosynthetic layers were clarified. It was found that increasing the number of geosynthetic layers extended the active shear zone in soft clay.

KEYWORDS: Geosynthetics, Embankment, Centrifuge model test, Progressive failure, Deformation

REFERENCE: Zheng, G., Xia, B., Zhou, H., Yu, X., Diao, Y. and Du, Y. (2024). Centrifuge modelling of the progressive failure of geosynthetic-reinforced embankments. *Geosynthetics International*, **31**, No. 5, 680–693. [https://doi.org/10.1680/jgein.23.00061]

1. INTRODUCTION

The application of geosynthetics is considered an effective and economical method for enhancing the stability of embankments over soft foundations (Chai *et al*. 2002; BSI 2012; Esmaeili *et al*. 2018; UIC 2018; Mandhaniya *et al*. 2022). In practice, Rowe and Soderman (1985, 1987) preliminarily discussed design considerations for geosynthetic-reinforced embankments on undrained soft soil and reported the reinforcement mechanism of geosynthetic reinforcement. Later, studies (Sharma and Bolton 1996; Chai *et al*. 2002; Hinchberger and Rowe 2003; Li and Rowe 2008; Wang *et al*. 2011; Miao *et al*. 2014; Bhowmik *et al*. 2018; Esmaeili *et al*. 2018) were conducted to investigate the global performance of embankments reinforced by geosynthetics constructed on soft foundations under undrained and partially drained conditions and to develop design methods for

calculating their stability. Among these studies, investigations (Wang *et al*. 2011; Miao *et al*. 2014; Esmaeili *et al*. 2018) have attempted to describe the influence of reinforcement layers on the deformation and stability of the embankment, but the failure mechanism was seldom reported in prior work.

Zhang (1999) found that the principal stress increment distributions at different locations in the soft layer beneath embankments are different, with small shear stresses near the embankment toe and the maximum shear stress possibly closer to the embankment centreline. Recent studies (Chai and Carter 2009; Zhang and Wang 2010; Zhang *et al*. 2015; Zhu *et al*. 2016; Briggs *et al*. 2017) have demonstrated that the plastic shear strains in soft soil were gradually induced at several critical zones associated with various deformation modes, and unreinforced embankments tended to collapse progressively due to the large accumulation of plastic shear strain. The failure mechanism in geosynthetic-reinforced embankment was more complex due to the combined effect of embankment filling, foundation properties and reinforcement design (Koerner *et al*. 1987). Koerner *et al*. (1987) found that in the case of geosynthetic-reinforced embankment instability, shear failure occurred within the underlying soft soil, while tensile cracks were observed on the embankment surface. However, the formation mechanism of failure in geosynthetic-reinforced embankments is still unclear.

In this study, centrifuge testing and numerical modelling were performed to evaluate the geosynthetic-reinforced embankment failure mechanism and stability. The particle image velocimetry (PIV) technique was used to quantify the deformation of soft foundations. A laser displacement sensor was attached to the top plate of the experimental box to measure the displacement. The main objectives in this study are: (i) to demonstrate the influence of the geosynthetic layers and lengths on the failure mechanism and global stability of the reinforced embankment; (ii) to investigate the development of tensile strain in the geosynthetics and (iii) to reveal the deformation modes and the formation mechanism of the failure in the soft foundation.

2. CENTRIFUGE MODELLING

2.1. Experimental programme and set-up

The centrifuge tests presented in this paper were performed in the geotechnical centrifuge laboratory at the Tianjin Research Institute for Water Transport Engineering (TIWTE), Ministry of Transport (MOT), China. The centrifuge has an effective maximum capacity of 500 g-ton, a maximum acceleration of 250***g*** and a diameter of 10 m. The centrifuge is equipped with a computer-controlled four-axis robotic manipulator. Details of the centrifuge principle and relevant applications can be found in Schofield (1980). Relevant scaling laws in this study are summarised in Table 1.

Two idealised centrifuge model tests of embankments reinforced by one and two layers of geosynthetics were designed to study the performance of embankments constructed on soft ground. The tests were carried out at an acceleration of 40***g*** using a model container 1000 mm long, 290 mm wide and 1000 mm high. Figure 1 schematically shows the configuration of the model tests. Half of the embankment was simulated due to inherent symmetry. The thicknesses of the embankment filling, soft clay layer and silty clay layer were 200 mm, 375 mm and 225 mm, respectively (i.e. 8 m, 15 m and 9 m prototypes). The embankment slope ratio was 1 : 1.5. The geosynthetic layers were applied to the entire width of the embankment in both tests. The geosynthetic reinforcement, measuring 459 mm (18.4 m in the prototype), was positioned 7.5 mm (0.3 m in the prototype) above the soft soil surface in the case of a single layer of reinforcement. In the scenario of two layers of geosynthetics, the upper layer was placed 7.5 mm above the lower layer. The lower layer was 459 mm long (18.4 m in the prototype), while the upper layer was 448 mm long (18 m in the prototype). In addition, a laser displacement sensor was attached to the top plate of the box to measure the surface displacement of the soft foundation 100 mm (4 m in the prototype) from the embankment toe.

Table 1. Main scale factors in centrifuge modelling (Schofield 1980; Zhou *et al.* 2019)

Items	Scaling factor (model/prototype)
Acceleration (m/s^2)	N
Length (m)	$1/N$
Displacement (m)	$1/N$
Density (kg/m^3)	1
Unit weight (N/m^3)	N
Strain	1
Stress (kPa)	1
Secant modulus (kN/m)	$1/N$
Tensile force (kN/m)	$1/N$

2.2. Soil properties

A layer of kaolin clay consolidated in one dimension was used as the model soft clay layer in the centrifuge tests to achieve a homogeneous model layer with known material and mechanical properties, a known stress history and a repeatable preparation procedure. Before pouring the kaolin clay slurry into the model container, the sides of a dismountable box were covered with a layer of silicon grease to reduce the friction between the walls and the clay during consolidation. After the kaolin clay slurry was placed into the container, one-dimensional consolidation at 1***g*** was performed. The metal loading plate was carefully placed on top. Five levels of loading were applied on top of the clay surface (10, 20, 40, 70 and 100 kPa). On completion of the loading steps and consolidation of the clay, the loading plate was unloaded. Subsequently, consolidation was conducted at 40***g*** to reach the prototype stress field. The soft clay layer was trimmed to produce a thickness of 375 mm after consolidation.

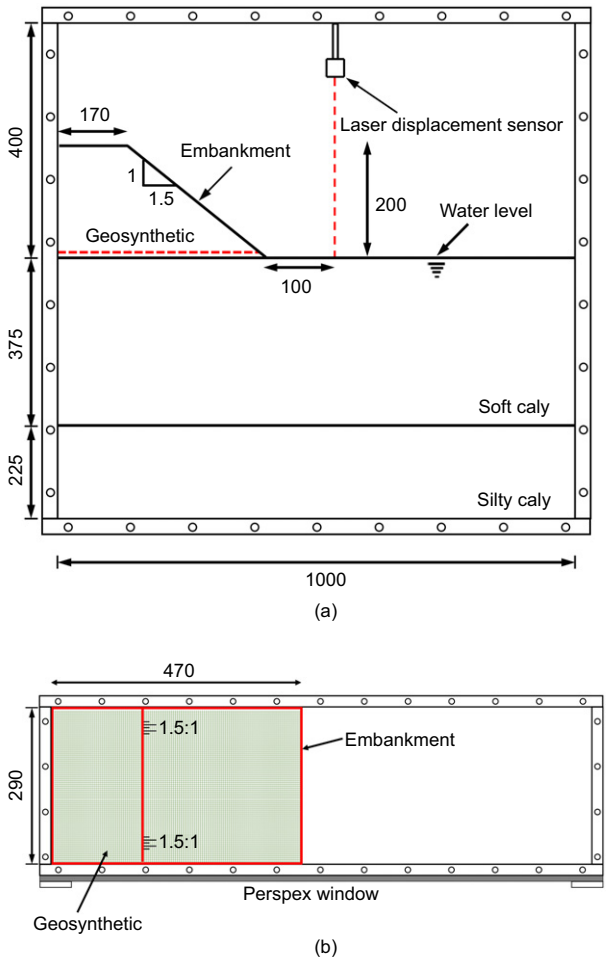

Figure 1. Schematic view of embankment model (units: mm): (a) side view; (b) plan view

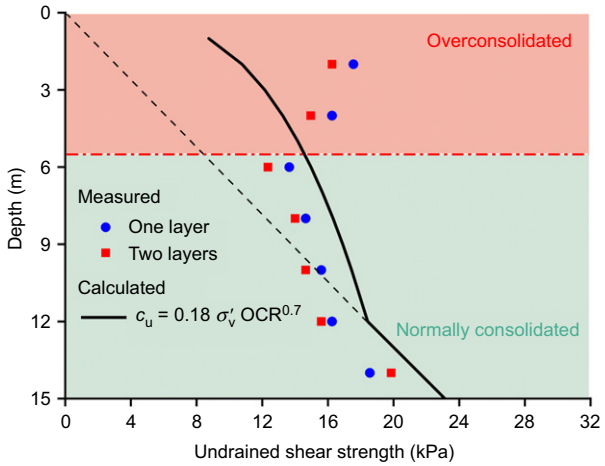

Figure 2. Undrained shear strength profile of soft clay (depth in prototype)

Due to the preconsolidation at 1***g*** and the self-weight consolidation in the centrifuge, the model ground had a thin layer of overconsolidated clay underlain by a thick layer of normally consolidated clay. Figure 2 shows the measured undrained shear strength profile of the soft clay. An estimated empirical relationship suggested by Randolph *et al.* (2009) was included for comparison, as follows:

$$c_u = 0.18\sigma'_v \mathrm{OCR}^{0.7} \quad (1)$$

where σ'_v is the vertical effective stress and OCR denotes the overconsolidation ratio.

The kaolin clay had a unit weight of 17.90 kN/m^3. The specific gravity of the kaolin clay used for all the experiments was 2.6. The liquid limit was 48.5% and the plastic limit was 29.8% (Hong and Wang 2016; Liu *et al.* 2019, 2023).

The underlying stratum was a typical soil deposit in Tianjin, China. Silty clay with a water content of 25% was compacted into the container. The centrifuge was spun to consolidate the silty clay at 40***g*** and then stopped when the measured settlement was stable. To achieve a bulk unit weight of 19.50 kN/m^3, a specified weight of soil was calculated for each 3 cm layer and compacted in the predefined volume.

Dry Toyoura sand with well-known engineering properties was adopted for embankment filling. This consisted of particles with a mean diameter of 0.17 mm, a maximum void ratio of 0.985, a minimum void ratio of 0.611, a specific gravity of 2.65 and an angle of friction at the critical state of 31°. The grain size distribution curve of Toyoura sand can be found in Ishihara (1993). In this study, the sand mass was recorded by the digital scale during construction and the average dry density of embankment filling was 1508 kg/m^3, corresponding to a relative density of 58.3%, ultimate friction angle of 42.25° and dilatancy angle of 11.96° (Bolton 1987; He *et al.* 2019; Nie *et al.* 2023; Zhou *et al.* 2023a, 2023b).

2.3. Geosynthetic material

In this study, high-density polyethylene (HDPE) material was used to model the geosynthetic reinforcement. To properly scale between the model and field prototype, two aspects of geosynthetic behaviour need to be considered: the tensile strength–strain characteristics and the soil–geosynthetic interface behaviour (Fan *et al.* 2019; Ye *et al.* 2020; Liu *et al.* 2021; Zheng *et al.* 2023a). The tensile tests were conducted in a tensile testing machine with the sample aspect ratio in accordance with ASTM D4595 (2 : 1). Global strains measured using the machine output were used to determine the impact of the clamps and any edge restraint effects (Sharma and Bolton 1996; Da Silva 2018). The corresponding results are presented in Figure 3 to determine the material stiffness and strength. For a secant prototype stiffness of 5% strain ($J_{5\%}$) and ultimate global strain (ε_u) of approximately 11%, respectively, the corresponding prototype had a tensile strength of 118 kN/m. The chosen HDPE provided a realistic approximation of materials commonly available for use in engineering applications.

Interface shear tests under four different normal stresses were conducted to determine the interfacial strength between the geosynthetic and embankment sand (Shen *et al.* 2020; Zheng *et al.* 2023b). Shearing was carried out at a rate of 1 mm/min, and the test results showed that the interface angle was 26.2°, which resulted in a reduced interface factor of 0.82 between the embankment sand and the geosynthetic.

2.4. Particle image velocimetry

For the centrifuge model tests, the movement of the soil was measured using PIV analysis of images captured by photogrammetry cameras with photogrammetry correction. As shown in Figure 4, an artificial texture was added to the edge of the clay liner using coloured sand to enable tracking during PIV. To capture digital images of the soil during the centrifuge tests, digital cameras with a maximum resolution of 3840 × 2748 pixels were installed at a height of 640 mm in front of the Perspex window. A close-range photogrammetric technique and the MATLAB-based software PIVlab (Thielicke and Sonntag 2021) were used.

2.5. Geosynthetic monitoring and installation

Figure 5 presents the installation details of the geosynthetic reinforcement. The geosynthetic was aligned with the flat backfill sand layer (see Figure 1(a)), and markers were applied to the geosynthetic 50 mm (2 m in the prototype) from the centre. These L-shaped markers were used to determine the strain sustained along the reinforcement layer throughout the test and at failure by tracking the movement of each marker through image analysis (Viswanadham and König 2009). Greased polyvinyl alcohol films were bonded to markers with one-to-one correspondence and were applied at the front of the container at the Perspex viewing window to protect the markers from being covered by sand during construction. An anchor rod with two sliding blocks was used to limit the horizontal movement of the geosynthetic reinforcement adjacent to the centre of the embankment while

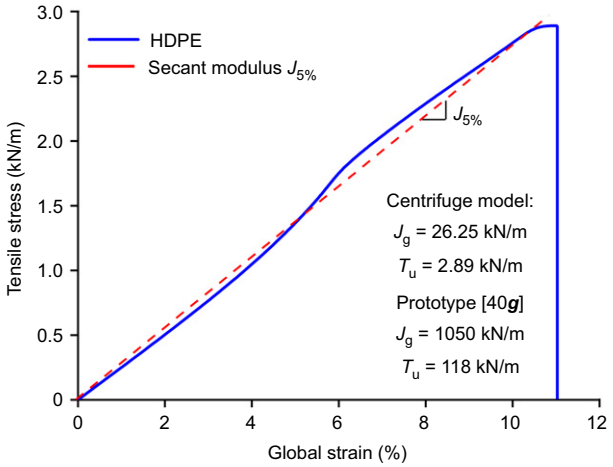

Figure 3. Stress–strain behaviour of geosynthetic material (200 mm width specimen test at a strain rate of 1 mm/min)

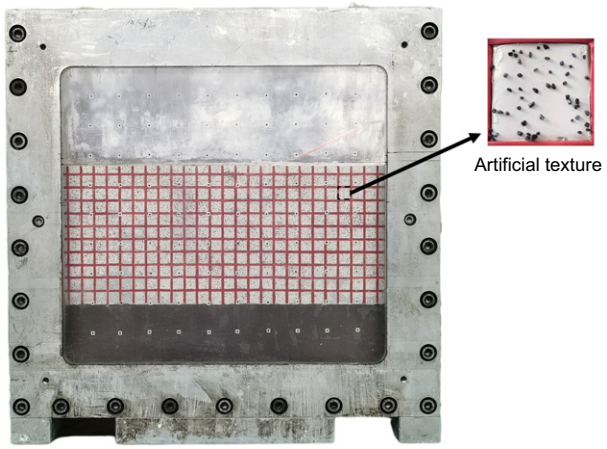

Figure 4. Artificial texture set-up

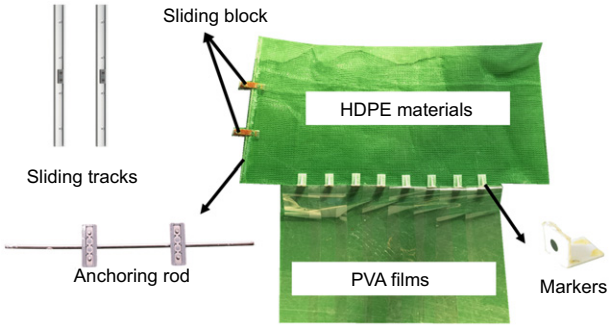

Figure 5. Geosynthetic instrumentation in centrifuge test

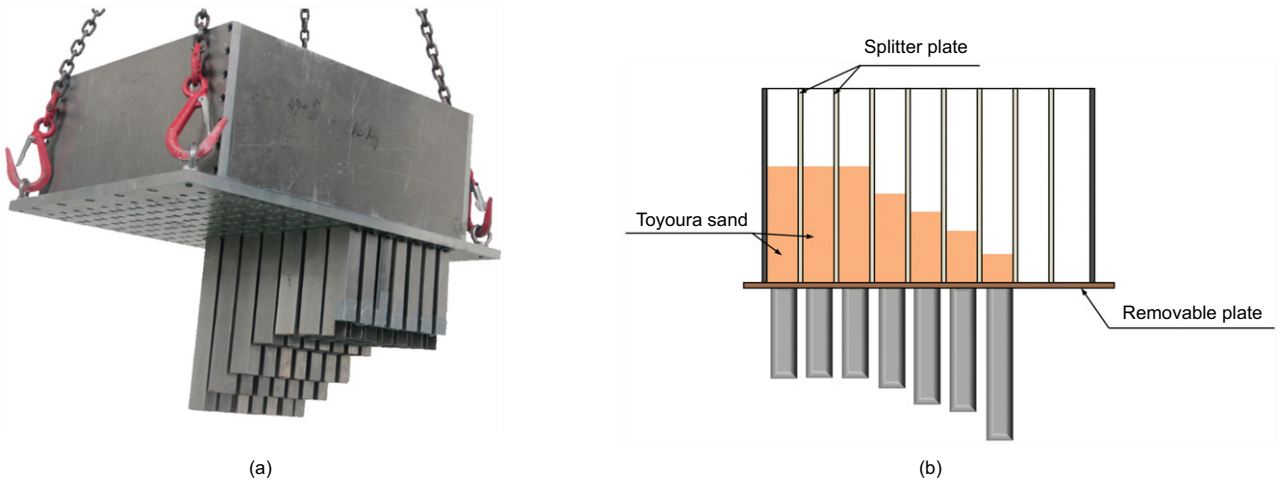

Figure 6. In-flight sand hopper: (a) stereogram; (b) elevation view

allowing downward vertical movement following the settlement of the soft soil foundation to achieve a plane strain boundary condition (Sharma and Bolton 1996; Li *et al.* 2021; Zhang *et al.* 2021).

2.6. Test schedule and procedure

For the centrifuge tests, an in-flight sand hopper was developed and used to simulate embankment construction with the sand rainfall technique at 40***g***. The technique, first introduced by Beasley and James (1976), has been increasingly used in geotechnical centrifuge model tests (Nguyen 2016; Nguyen *et al.* 2016). The cubic box of the sand hopper had internal dimensions of 720 mm × 280 mm × 270 mm, as shown in Figure 6(a). The hopper was divided into seven cells to adjust the thickness of the embankment slope. Specifically, the minimum length was approximately 30 mm at the toe side of the embankment, while the maximum length was approximately 200 mm at the centre of the embankment, as shown in Figure 6(b). In other cells, the thickness increased gradually from the toe side to the centre of the embankment according to the targeted embankment slope (1.5H : 1V). Due to the inertia force (i.e. Coriolis force) during rotation of the centrifuge (from the window side to the rear side of the container), the thickness of sand in the hopper was adjusted to be 10 to 15 mm higher than that in the rear side. An electrical control system was set up in a control room to open and close the valve, which was used to simulate rainfall from the sand hopper. To simulate the construction of embankments in practice, the construction speed of the embankment was 13.3 mm/min at 40***g*** and that of the corresponding prototype was 0.57 m/day.

After preparing the model ground, the sand hopper was assembled at the top left of the model container, as shown in Figure 7. The completed centrifuge assembly for a sand test, involving all the components described (sand rainfall and control system, completed soil, geosynthetic model, instrumentation and in-flight sand hopper), is presented in this photograph. The testing programme was designed to observe the deformation of the model ground as well as the displacement of the improved area when constructing the embankment. The centrifuge acceleration was gradually increased to the 40***g*** level, pausing after each additional 10***g***. After the soft foundation model stabilised at the 40***g*** level, the construction process was started.

3. CENTRIFUGE RESULTS

The results in this section focus on the soft clay layer displacement and geosynthetic tensile strain characteristics during embankment construction. The vertical displacement near the embankment toe and geosynthetic tensile strain were directly measured by the laser displacement sensor and L-shaped markers, respectively. The centrifuge model test results are given at the prototype scale.

3.1. Displacement observations

Figure 8 presents the uplift of the ground surface 100 mm (4 m in the prototype) from the embankment toe. During construction, the displacement gradually accumulates from the beginning until the embankment collapses, and the corresponding curve shows a nonlinear trend. Once the soft foundation approaches the failure state, the uplift greatly increases. To quantify the collapse height of the two cases, the methods proposed by Villalobos Jara (2006)

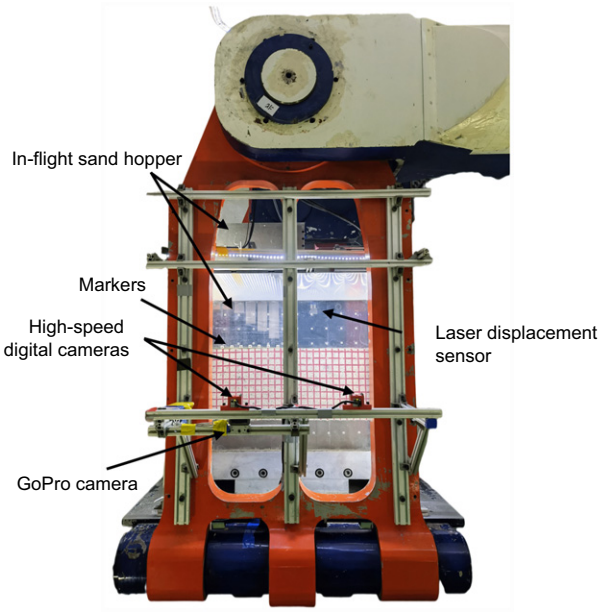

Figure 7. Centrifuge model and instrumentation in in-flight construction

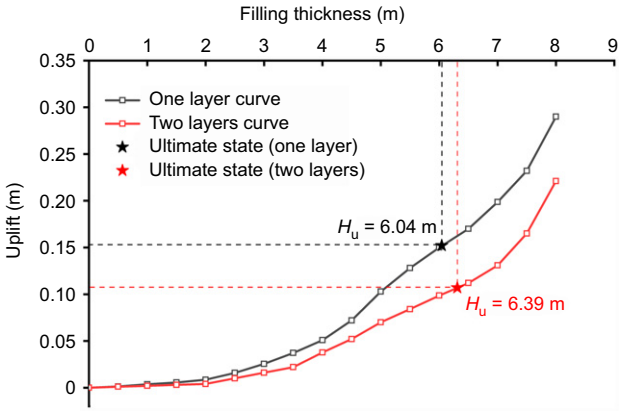

Figure 8. Relationship between filling height and vertical displacement 100 mm (4 m in protype) away from the embankment toe

Table 2. Comparison between centrifuge tests and existing design method on the collapse height of reinforced embankments

Reinforcement type	Collapse height (m) (centrifuge tests)	Collapse height (m) (Hinchberger and Rowe 2003)	Difference (%)
One layer	6.04	6.25	8.6
Two layers	6.39	6.44	4.92

and Wang *et al.* (2018) were adopted. Yield was determined as the intersection of the two straight lines that fit the load–displacement curve at the beginning and the end of the curve.

To verify the current centrifuge model results, the collapse height of two centrifuge tests is compared with the existing design method proposed by Hinchberger and Rowe (2003). In their study, the design method is applied

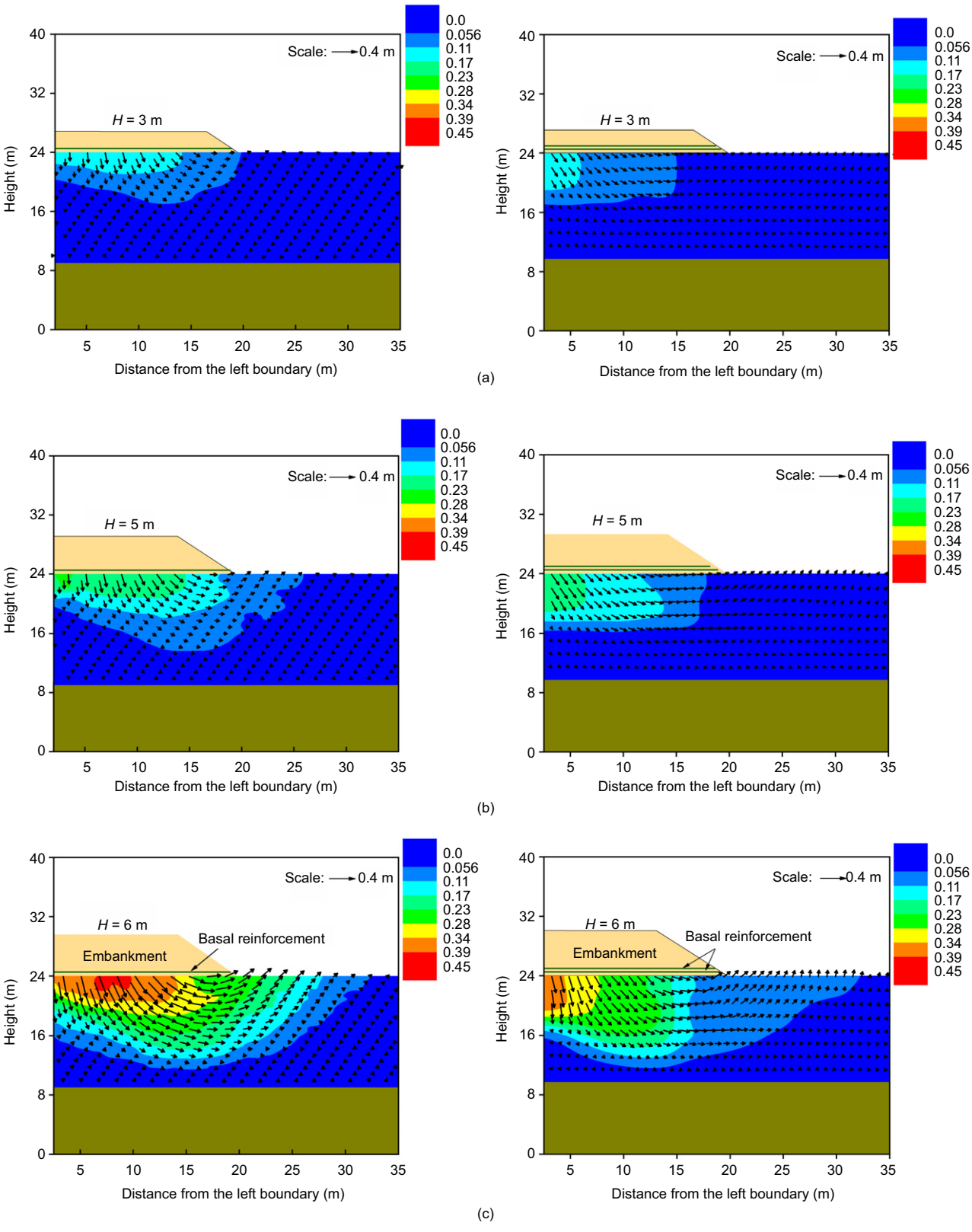

Figure 9. Displacement vectors and global displacement contours of geosynthetic-reinforced embankment for cases with one layer and two layers: (a) $H = 3$ m; (b) $H = 5$ m; (c) $H = 6$ m

to calculate the stability of geosynthetic-reinforced embankments on soft clay foundation soil with increasing undrained shear strength with depth. The comparison results in Table 2 demonstrate good agreement between the results determined in this work and those of the existing design method. Furthermore, the deformation pattern and distribution of displacement vectors exhibit consistent results with the previous centrifuge test findings conducted by Sharma and Bolton (1996). This confirms the reliability and precision of the centrifuge models.

During the test, the global displacement behaviours of the soft foundation were continuously observed via PIV. Figure 9 shows the displacement vectors and global displacement contours of the geosynthetic-reinforced embankment under different filling heights. The major displacement that occurs inside the embankment shoulder is dominated by vertical subsidence, while the displacement vectors beyond the embankment toe exhibit an upward tendency. In general, the displacement magnitude of the embankment reinforced with two layers of geosynthetics is much smaller than that reinforced with one layer. Additionally, the distributions of the vectors in the soft clay layer of the two cases are different. Compared with one layer of reinforcement, two layers obviously limit the horizontal displacement of soft soil, especially between the embankment shoulder and toe. In addition, as the critical filling height is nearly achieved, as shown in Figure 9(c), the displacement increments of the embankment reinforced by two layers of geosynthetics are much smaller than those of the embankment reinforced by one layer.

3.2. Tensile strain of geosynthetics

Figure 10 shows the global tensile strain distributions of the model geosynthetics along the transverse direction of the embankment at different filling heights. In the initial stage of construction (i.e. Figure 10(a)), a limited strain is observed for both cases. A significant increase in tensile strain is found between the centreline and the shoulder of the embankment with increasing filling height, followed by continuously decreasing strains along the embankment. Finally, the test ends with almost no strain at the toe of the embankment. This distribution of the geosynthetic strain is mostly caused by the self-weight of the embankment fill being larger in the centre and smaller in the side slope. For the two-layer case, a more sufficient reduction in lateral spreading and a limited increase in lateral earth pressure develops under construction, resulting in smaller strains of the geosynthetics between the centreline and the shoulder of the embankment. After the centrifuge tests, the embankment filling soil was excavated to confirm the failure mode of the geosynthetics. The appearance of deformed geosynthetics is shown in Figure 10(c). Tensile failure occurs in the one-layer case, closest to the centreline of the embankment. This phenomenon is consistent with the measured results.

3.3. Failure mechanism

3.3.1. *Shear strain development*

In this study, the maximum shear strain is used to describe the failure mechanism in the soft foundation under the embankment load. The maximum shear strain Υ is defined as the second invariant of the deviatoric strain tensor (Higo *et al.* 2015; Yuan *et al.* 2018; Yang *et al.* 2019; Keawsawasvong and Ukritchon 2019a, 2019b; Yodsomjai *et al.* 2021).

Figure 11 shows the development process of shear strain Υ in the soft clay at filling heights of 3 m, 5 m and 6 m for one and two layers of geosynthetics. For one layer of geosynthetic, the initial shear strain occurs in three regions: the centreline of the embankment, the embankment shoulder and the embankment toe in the foundation. The zone of shear strain spreads both forward and backward from the starting point until a failure slip surface is formed. For the case of two layers of geosynthetics (see Figure 11(b)), the shear strain initially arises at the centreline of the embankment in the first phase and develops beyond the embankment toe.

3.3.2. *Displacement development*

The use of typical points to examine the deformation behaviour of slopes and foundations has been successfully employed in prior investigations (Zhang and Wang 2010; Zhang *et al.* 2015, 2017; Luo *et al.* 2020). In this study, three typical points located on the slip surface were chosen to examine the deformation behaviour of soft clay. The numbers in the brackets illustrate the horizontal and vertical coordinates of typical points, as shown in Figure 12.

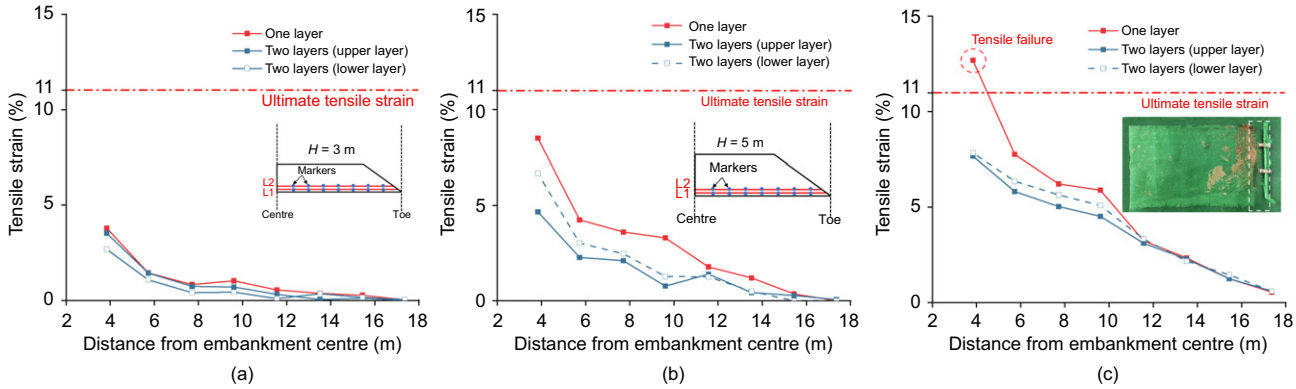

Figure 10. Tensile strain of geosynthetics for cases with one layer and two layers: (a) $H = 3$ m; (b) $H = 5$ m; (c) $H = 6$ m

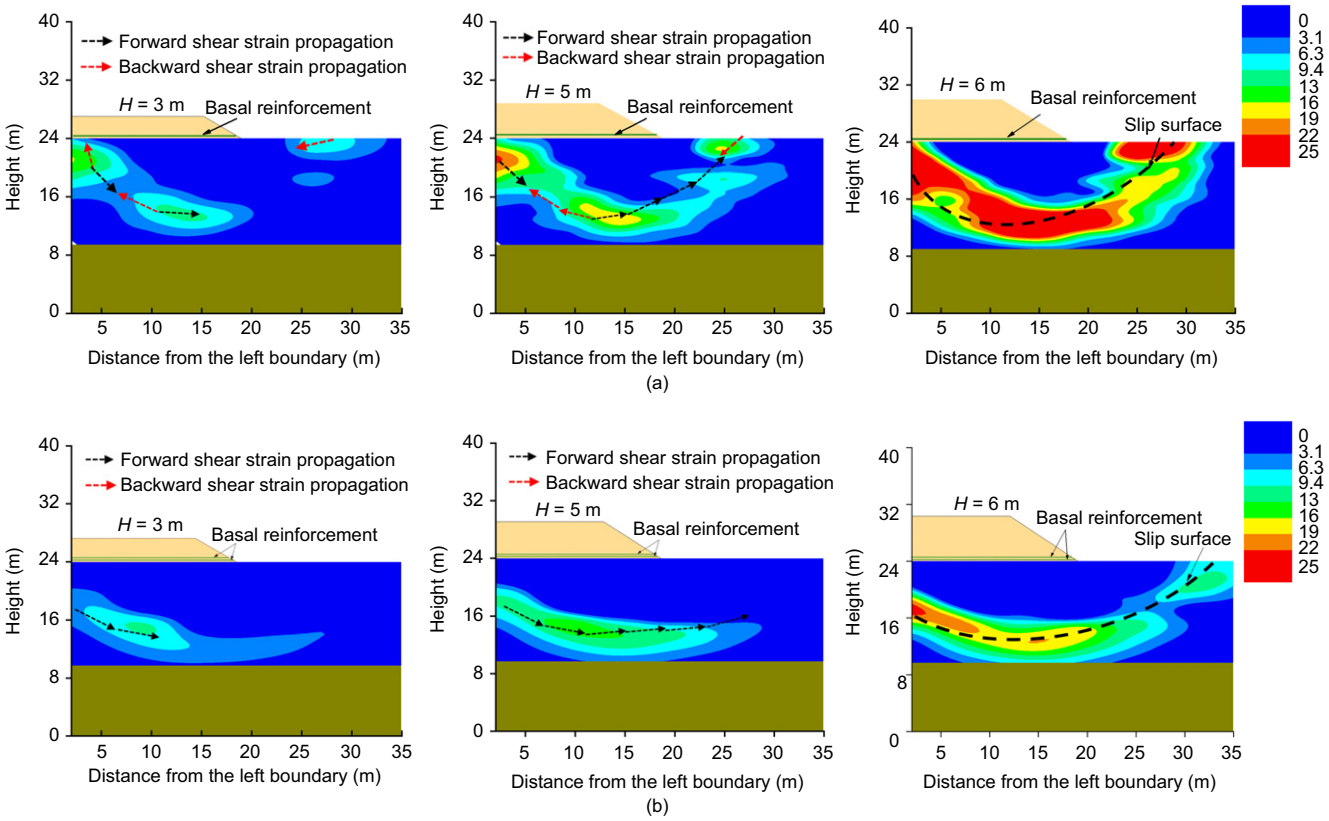

Figure 11. Shear strain of clay layer for cases with: (a) one layer; (b) two layers (unit: %)

Figures 12(b) and 12(c) show the horizontal and vertical displacement histories of three typical points for different reinforcement conditions. The displacements of all the typical points increased during construction. Additionally, each displacement curve corresponds to a turning point. The displacement histories can be divided into two stages by turning point, as shown by the dashed lines in Figure 12. A relatively small displacement is found in stage I and increases slowly. The displacement starts to accelerate significantly once entering stage II, followed by plastic zone penetration and embankment collapse. In the one-layer case (Figure 12(b)), the three typical points enter stage II almost simultaneously, while for the two-layer conditions (Figure 12(c)), the point underneath the embankment centre (e.g. point A) enters stage II earlier than the points under the embankment shoulder and toe (e.g. points B and C). In other words, the typical points successively enter stage II from the embankment centre to the toe. Such a development feature of displacement histories is consistent with the formation sequence of the shear strain development. In addition, as the number of geosynthetic layers increases, there is less subsoil settlement at the centreline of the embankment and less horizontal displacement away from the embankment shoulder, which limits the global displacement of the soft foundation and ensures the stability of the embankment.

4. NUMERICAL ANALYSES

Although the centrifuge tests revealed the deformation and failure mechanisms of geosynthetic-reinforced embankments, certain factors of the geosynthetic reinforcements, such as the number of geosynthetic layers and the length of the geosynthetic, have been disregarded. Therefore, a numerical model was established using ABAQUS finite element software for further investigation (Liu *et al.* 2007; Mandhaniya *et al.* 2022; Wang *et al.* 2023). The calculation scenarios are summarised in Table 3.

4.1. Numerical modelling

Due to the symmetrical cross-sectional design, it was determined that modelling only half of the embankment would be adequate. The simulated geosynthetic-reinforced embankment system dimensions were in line with the scaled-up prototype, which were obtained from centrifuge tests conducted at accelerations of up to 40***g***.

The configuration and mesh of the numerical model are depicted in Figure 13. The side boundaries were subjected to constraints for horizontal displacement (in the x and y directions), while a rough, rigid boundary with zero displacement in all three directions was simulated at the base of the soft foundation. To capture the coupled behaviour of soft foundations, 8-node hexahedral elements with linear displacement and pore pressure degrees of freedom (C3D8P) were employed.

Table 4 presents the soil constitutive models and their corresponding material properties. The silty clay layer and embankment were modelled as linear elastic and perfectly plastic materials, respectively, using the Mohr–Coulomb failure criterion. Meanwhile, the soft clay layer was represented by a modified Cam–Clay model (MCC). Based on undrained triaxial compression stress paths, the MCC model determined the undrained

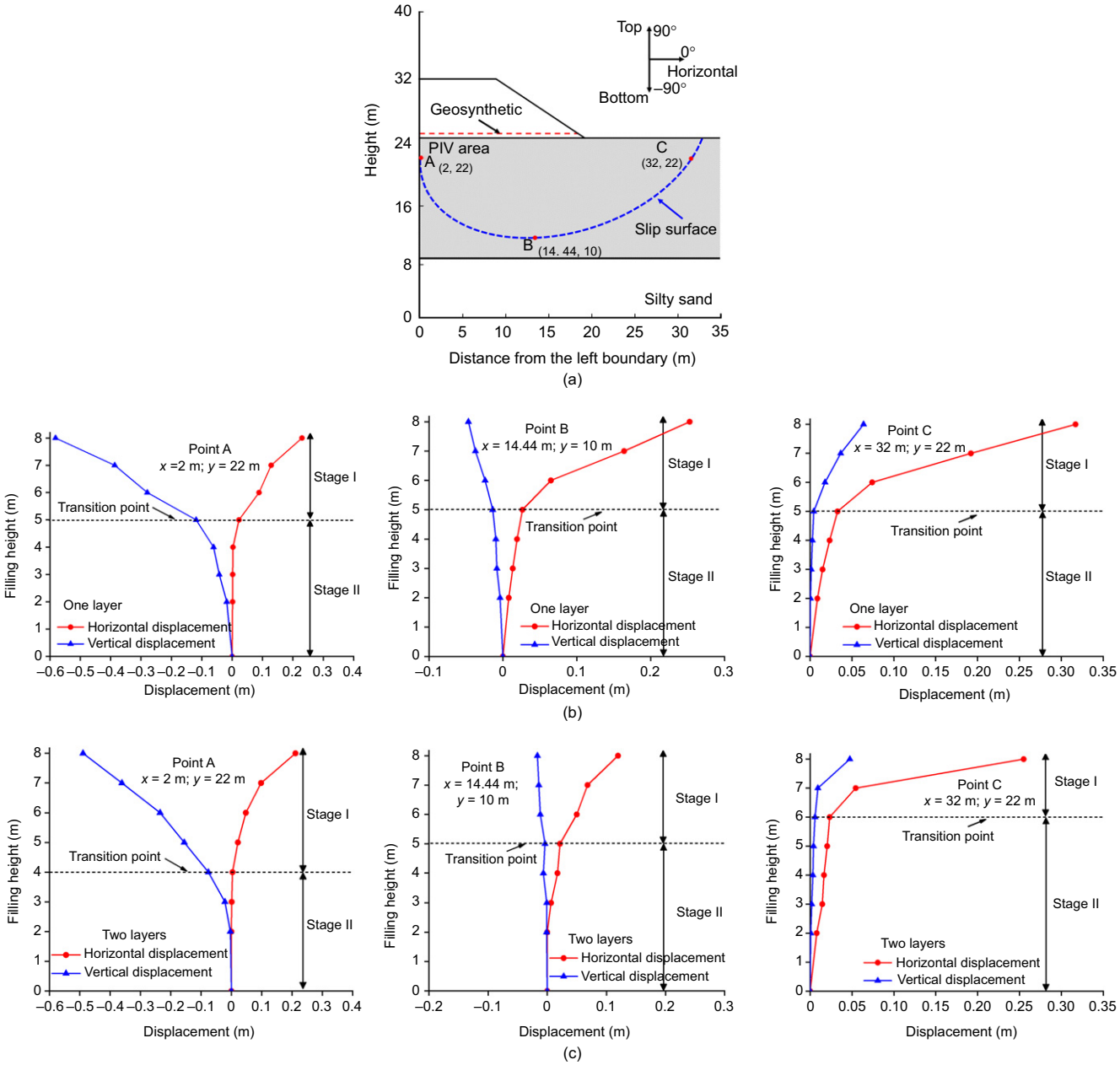

Figure 12. Displacement histories of typical points for different layers of reinforcement during construction (unit: m): (a) schematic view and location of typical points (b) displacement histories of one layer; (c) displacement histories of two layers

Table 3. Values of the geosynthetic reinforcement parameters

Case no.	Number of geosynthetic layers	Length of geosynthetic
1	0	—
2	1	18.4 m (covering whole embankment width)
3	2	2.4 m, 4.8 m, 7.2 m, 9.6 m, 12 m, 14.4 m, 16.8 m, 18.4 m

shear strength (c_u) according to the following equation (Liu *et al.* 2007).

$$c_u = \frac{M}{2}\exp\left\{\frac{e_1 - (\lambda - \kappa)\ \mathrm{In}\ 2}{\lambda} - \frac{e_0}{\lambda}\right\} \quad (2)$$

The strength parameter is denoted as M. The slope of the consolidation line is determined by λ and the swelling line slope is indicated by κ. The initial isotropic consolidation line originates from point e_1, and e_0 corresponds to the initial void ratio, which is influenced by the initial stress state. Parameters such as λ, κ and e_1 can be derived from one-dimensional compression tests, providing valuable insights. Most of the soil parameters employed in the numerical modelling were consistent with those adopted in the centrifuge model tests.

The geosynthetic reinforcements were modelled using 4-node linear elastic membrane elements (M3D4). Interface elements were applied between the embankment fill and the reinforcements. The interfaces in this study were simulated using the master–slave contact pairs available in ABAQUS software. To accurately represent the interaction at the

interface, the well-established Coulomb friction model was employed. Following previous approaches, the friction angle at the column–soil interface was assumed to be equal to the effective friction angle of the filling.

Before proceeding to further analysis, the numerical simulation was validated by comparison with the prior results. Figure 14 presents the uplift comparisons of the ground surface 4 m from the embankment toe in case No. 2. From a numerical viewpoint, the uplift of the ground surface exhibits consistent variations with the centrifuge test results, and the critical filling height from the numerical modelling aligns with both the test and the existing design results, which further confirms the validity of the numerical model and its parameters.

4.2. Effect of reinforcement length on global stability

Figure 15 illustrates the impact of geosynthetic reinforcement length on overall stability. The length of the two layers of reinforcements varies from 2.4 m to 18.4 m. The curve representing the ultimate filling height can be divided into two stages. Initially, during phase I, the reinforcements do not significantly affect stability. However, once phase II is reached, there is a rapid increase in stability. Additionally, Figure 15 also highlights the ultimate filling height in case No. 2 for comparison. It is evident that using two layers of reinforcements with a length of 16 m is more effective than using a single layer covering the entire width of the embankment.

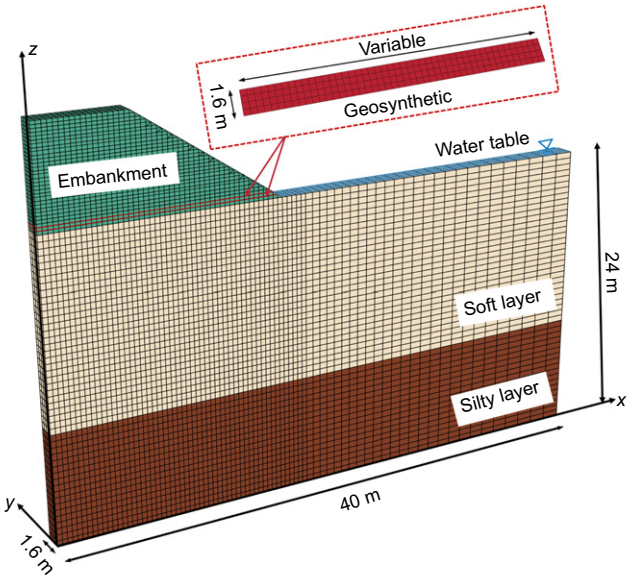

Figure 13. Finite element mesh used for numerical modelling

5. DISCUSSION

5.1. Distribution of the strain components in the soft foundation

Combined with the centrifuge and numerical modelling results, the distribution of various strain components in the soft foundation during construction can be observed. The components include the vertical strain component ε_{yy} and the shear strain component ε_{xy}, as depicted in

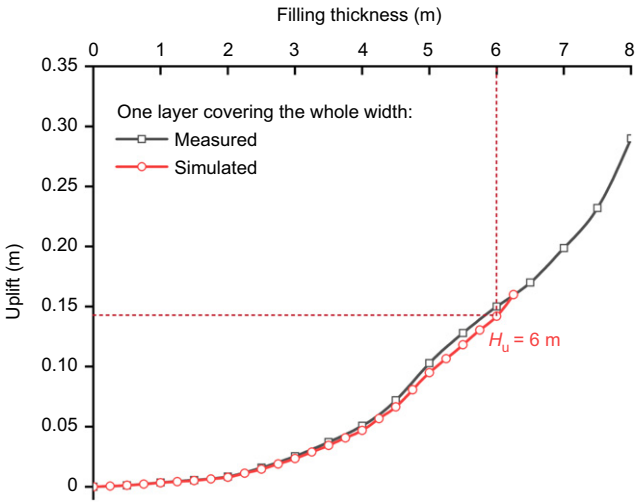

Figure 14. Comparison of ground surface uplift between centrifuge test and numerical analysis

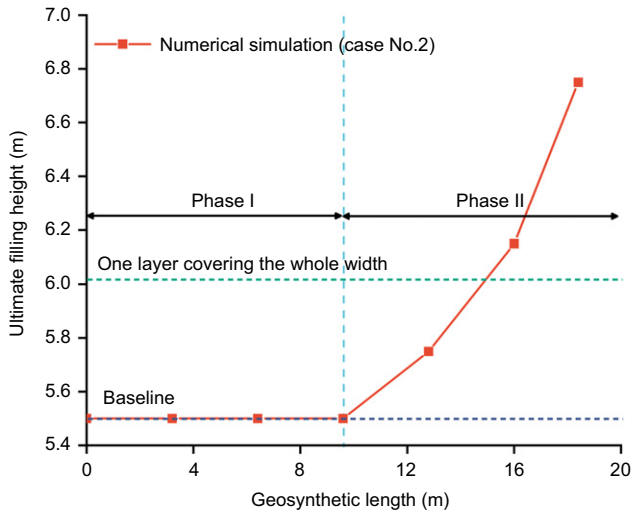

Figure 15. Variation in ultimate embankment filling height with various geosynthetic lengths

Table 4. Physical property values used for numerical analysis

Material	ν	c_u (kPa)	E (MPa)	ϕ' (°)	γ (kN/m^3)	λ	κ	M	e_1	e_0
Soft clay	0.35	—	—	—	18	0.26	0.05	1.02	3.27	varies
Silty clay	0.25	20	37.5	35	19.5	—	—	—	—	—
Filling	0.3	0	30	42.25	15.08	—	—	—	—	—
Geosynthetic	$J_{5\%}$ = 1050 kN/m, t = 3 mm, ν_{geo} = 0.3									

Figure 16. The soft foundation beneath the embankment centre is mainly subjected to vertical compressive stress during construction. With increasing filling height, the vertical strain component (ε_{yy}) gradually accumulates, indicating that the soft clay undergoes significant settlement. Near the toe of the embankment, the soft soils are influenced by lateral earth pressure, and the accumulated strains are mainly tension and cause a remarkable uplift.

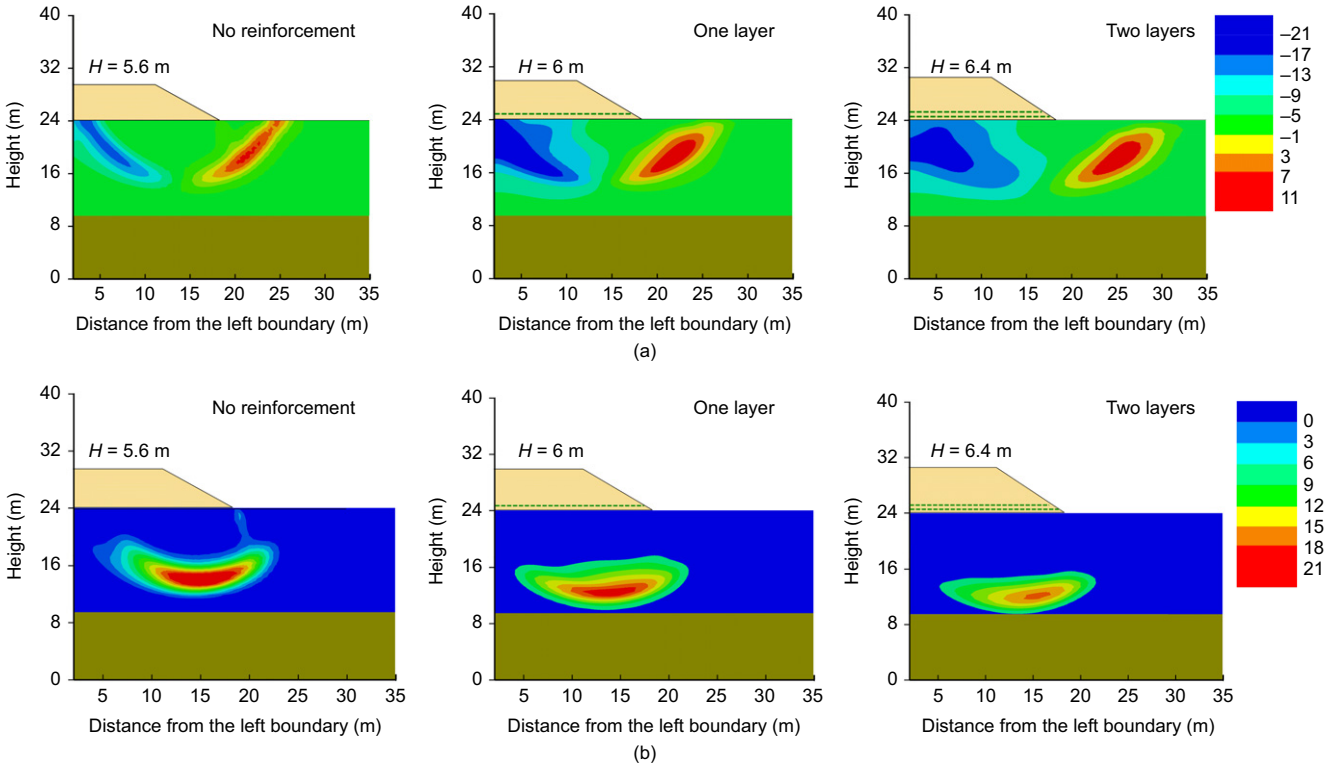

Figure 16. Contours of strain components with different reinforcement layers (unit: %): (a) ε_{yy}; (b) ε_{xy}

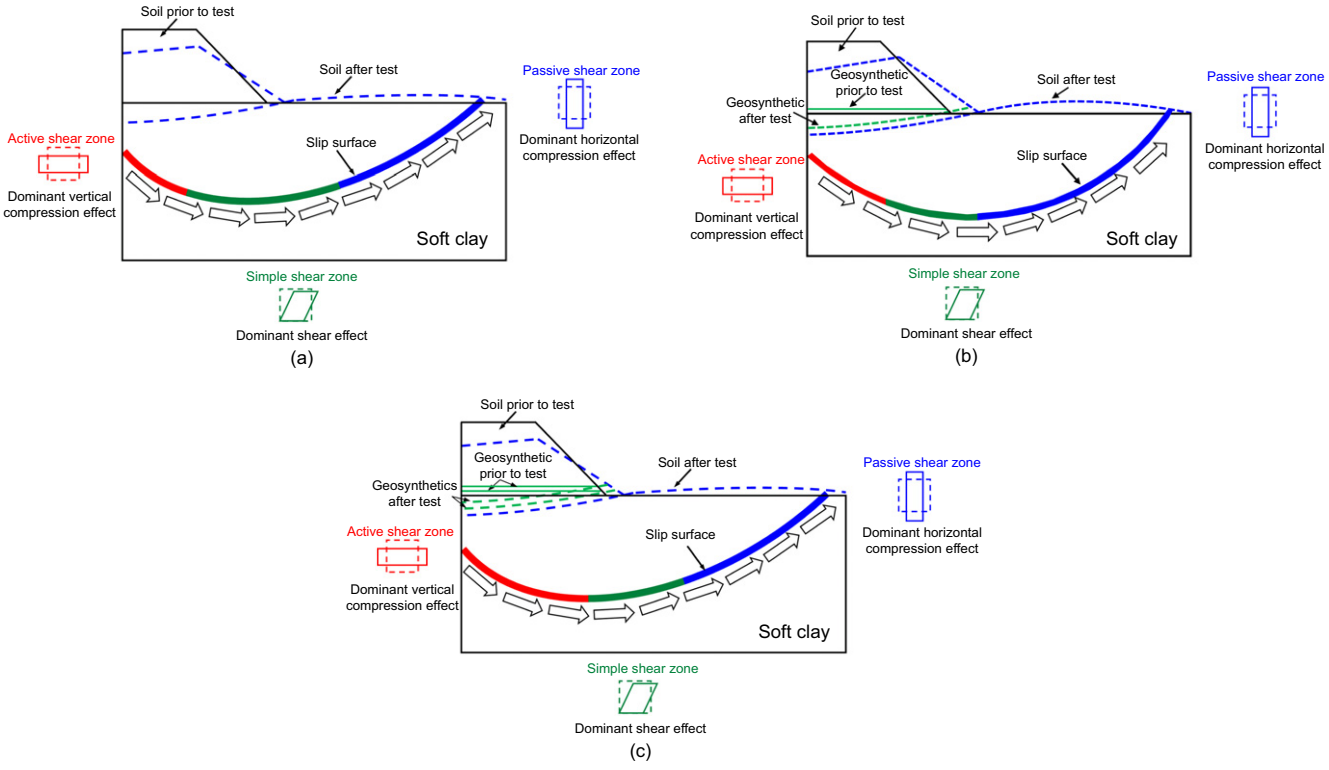

Figure 17. Deformation modes of embankment reinforced by different numbers of layers of geosynthetics: (a) no reinforcement; (b) one layer; (c) two layers

In addition, the shear strain component accumulation is mainly observed in the relatively deep areas of the soil foundation, where large movement is induced in the horizontal direction. The use of geosynthetics significantly reduces the accumulation of tension and shear strain components due to the formation of a limited lateral earth pressure in the soft soil.

5.2. Deformation mode of geosynthetic-reinforced embankment

Figure 17 shows the deformation modes of the embankment reinforced by different numbers of layers of geosynthetics. Different zones of a potential slip surface formed beneath embankments are associated with various shear modes.

- In active shear zones, plastic shear strains are induced by vertical compression (i.e. beneath the centreline of the embankment). The deformation mode in this zone is similar to triaxial compression.
- Obvious direct shear deformation is observed in the simple shear zone. The deformation mode in this area is considered direct shear.
- The passive shear zone is near the toe of the slip surface, where shearing is induced by increasing horizontal stress, and the deformation mode in this zone is analogous to triaxial extension.

The embankment fails when shear failure occurs and a near-circular critical slip surface gradually forms. However, the size of the characteristic deformation zone changes with the number of geosynthetic layers. For the two-layer case, the upper geosynthetic carries most of the lateral stress caused by the lateral spreading of the embankment, and the lower geosynthetic carries the remaining vertical load due to the tensioned membrane effect. Lateral stress reduction occurs above the subsoil and the area of soft clay yielding under vertical compressive stress is increased. Therefore, the active shear zone is extended, as shown in Figure 17(c).

6. CONCLUSIONS

Through a series of centrifuge model tests, this paper investigated the deformation and failure mechanism of geosynthetic-reinforced embankments constructed on soft clay foundations. The effect of the layers and lengths of geosynthetics, which were important factors influencing the global performance of the embankments, was analysed. The main findings are as follows.

(*a*) A progressive shear failure of the soft foundation rather than immediate collapse is observed in both cases studied. Shear strains in the soft foundation accumulate both forward and backward until a global slip surface develops. The shear strain for one geosynthetic layer first arises at the centreline, shoulder and toe of the embankment, while for two layers, it initially arises at the centreline and develops forward toward the embankment toe. Meanwhile, the geosynthetic material experiences tensile failure at the centreline of the embankment once it reaches its ultimate strain. In addition, using two layers of geosynthetics with a relatively short length is more effective than using a single layer covering the entire width of the embankment.

(*b*) The accumulation of shear strain in a potential slip surface that forms beneath an embankment is associated with various shear modes: shear strain under the embankment centre is induced by large compressive deformation (active shear zones); obvious direct shear deformation is observed between the embankment shoulder and toe (simple shear zone); shear strain caused by extension occurs out of the embankment toe (passive shear zone). Compared with the results in the no reinforcement and one-layer cases, a more sufficient restriction on lateral spreading and a smaller increment of lateral earth pressure develops in the two-layer case. As a result, the active shear zone in soft clay is extended.

ACKNOWLEDGMENTS

This research was funded by the National Natural Science Foundation of China (No. 52078337, No. 52008293, No. 52208363, No. 52322809 and No. 52078335), the Project of Tianjin Science and Technology Plan (No. 21JCZXJC00070), the Natural Science Foundation of Hebei, China (No. E2021202215) and the China National Postdoctoral Program for Innovative Talents (Grant No. BX20220225).

NOTATION

Basic SI units are shown in parentheses.

c_u	undrained shear strength of soft clay (Pa)
E	elastic modulus (Pa)
e_0	initial void ratio (dimensionless)
e_1	void ratio at unit pressure (dimensionless)
H	filling height (m)
H_u	ultimate filling height (m)
$J_{5\%}$	secant prototype stiffness of 5% strain of geosynthetic (N/m)
J_g	geosynthetic tensile stiffness (N/m)
M	slope of the critical state line (dimensionless)
OCR	over consolidation ratio (dimensionless)
T_u	ultimate tensile force of the geosynthetic (N/m)
t	thickness of geosynthetic (m)
γ	unit weight (N/m^3)
ε_u	ultimate global strain of geosynthetic (dimensionless)
ε_{xy}	shear strain component (dimensionless)
ε_{yy}	vertical strain component (%)
κ	slope of the swelling line (dimensionless)
λ	slope of the virgin consolidation line (dimensionless)

ν Poisson's ratio (dimensionless)
ν_{geo} Poisson's ratio of geosynthetic (dimensionless)
σ'_v vertical effective stress (Pa)
Υ maximum shear strain (dimensionless)
ϕ' effective friction angle (degree)

ABBREVIATIONS

C3D8P 8-node hexahedral elements with linear displacement and pore pressure degrees of freedom
HDPE high-density polyethylene
M3D4 4-node linear elastic membrane elements
MCC modified Cam–Clay model

REFERENCES

ASTM D4595: *Standard Test Method for Tensile Properties of Geotextiles by the Wide-Width Strip Method*. ASTM International, West Conshohocken, PA, USA.

Beasley, D. H. & James, R. G. (1976). Use of a hopper to simulate embankment construction in a centrifugal model. *Géotechnique*, **26**, No. 1, 220–226.

Bhowmik, R., Shahu, J. T. & Datta, M. (2018). Failure analysis of a geomembrane lined reservoir embankment. *Geotextiles and Geomembranes*, **46**, No. 1, 52–65.

Bolton, M. D. (1987). The strength and dilatancy of sands. *Géotechnique*, **36**, No. 1, 65–78.

Briggs, K. M., Loveridge, F. A. & Glendinning, S. (2017). Failures in transport infrastructure embankments. *Engineering Geology*, **219**, 107–117, https://doi.org/10.1016/j.enggeo.2016.07.016.

BSI (2012). BS 8006-1: Code of practice for strengthened/reinforced soils and other fills, incorporating Corrigendum 1. BSI, London, UK.

Chai, J. & Carter, J. P. (2009). Simulation of the progressive failure of an embankment on soft soil. *Computers and Geotechnics*, **36**, No. 6, 1024–1038.

Chai, J. C., Miura, N. & Shen, S. L. (2002). Performance of embankments with and without reinforcement on soft subsoil. *Canadian Geotechnical Journal*, **39**, No. 4, 838–848.

Da Silva, T. (2018). *Centrifuge Modelling of the Behaviour of Geosynthetic-Reinforced Soils Above Voids*, PhD thesis, University of Cambridge, Cambridge, UK.

Esmaeili, M., Naderi, B., Neyestanaki, H. K. & Khodaverdian, A. (2018). Investigating the effect of geogrid on stabilization of high railway embankments. *Soils and Foundations*, **58**, No. 2, 319–332.

Fan, K., Liu, S. H., Cheng, Y. P. & Wang, Y. (2019). Sliding stability analysis of a retaining wall constructed by soilbags. *Géotechnique Letters*, **9**, No. 3, 211–217.

He, Y., Liu, Y., Zhang, Y. & Yuan, R. (2019). Stability assessment of three-dimensional slopes with cracks. *Engineering Geology*, **252**, 136–144, https://doi.org/10.1016/j.enggeo.2019.03.001.

Higo, Y., Lee, C. W., Doi, T., Kinugawa, T., Kimura, M., Kimoto, S. & Oka, F. (2015). Study of dynamic stability of unsaturated embankments with different water contents by centrifugal model tests. *Soils and Foundations*, **55**, No. 1, 112–126.

Hinchberger, S. D. & Rowe, R. K. (2003). Geosynthetic reinforced embankments on soft clay foundations: predicting reinforcement strains at failure. *Geotextiles and Geomembranes*, **21**, No. 3, 151–175.

Hong, Y. & Wang, L. (2016). *Deformation and Failure Mechanism of Excavation in Clay Subjected to Hydraulic Uplift*. Springer, Berlin, Germany.

Ishihara, K. (1993). Liquefaction and flow failure during earthquakes. *Géotechnique*, **43**, No. 3, 351–451.

Keawsawasvong, S. & Ukritchon, B. (2019a). Undrained basal stability of braced circular excavations in non-homogeneous clays with linear increase of strength with depth. *Computers and Geotechnics*, **115**, 103180, https://doi.org/10.1016/j.compgeo.2019.103180.

Keawsawasvong, S. & Ukritchon, B. (2019b). Undrained stability of a spherical cavity in cohesive soils using finite element limit analysis. *Journal of Rock Mechanics and Geotechnical Engineering*, **11**, No. 6, 1274–1285.

Koerner, R. M., Hwu, B. L. & Wayne, M. H. (1987) Soft soil stabilization designs using geosynthetics. *Geotextiles and Geomembranes*, **6**, No. 1, 33–51.

Li, A. L. & Rowe, R. K. (2008). Effects of viscous behavior of geosynthetic reinforcement and foundation soils on the performance of reinforced embankments. *Geotextiles and Geomembranes*, **26**, No. 4, 317–334.

Li, L. Y., Rajesh, S. & Chen, J. F. (2021). Centrifuge model tests on the deformation behavior of geosynthetic-encased stone column supported embankment under undrained condition. *Geotextiles and Geomembranes*, **49**, No. 3, 550–563.

Liu, H. L., Ng, C. W. & Fei, K. (2007). Performance of a geogrid-reinforced and pile-supported highway embankment over soft clay: case study. *Journal of Geotechnical and Geoenvironmental Engineering*, **133**, No. 12, 1483–1493.

Liu, S., Fan, K. & Xu, S. (2019). Field study of a retaining wall constructed with clay-filled soilbags. *Geotextiles and Geomembranes*, **47**, No. 1, 87–94.

Liu, S. H., Liao, J., Bong, T. T. & Fan, K. W. (2021). Repeated loading of soilbag-reinforced road subgrade. *Geosynthetics International*, **28**, No. 2, 113–124.

Liu, W., Liang, J. & Xu, T. (2023). Tunnelling-induced ground deformation subjected to the behavior of tail grouting materials. *Tunnelling and Underground Space Technology*, **140**, 105253, https://doi.org/10.1016/j.tust.2023.105253.

Luo, F., Huang, R. & Zhang, G. (2020). Centrifuge modeling of the geogrid-reinforced slope subjected to differential settlement. *Acta Geotechnica*, **15**, No. 10, 3027–3040.

Mandhaniya, P., Shahu, J. T. & Chandra, S. (2022). Numerical analysis on combinations of geosynthetically reinforced earth foundations for high-speed rail transportation. *Structures*, **43**, 738–751, http://dx.doi.org/10.1016/j.istruc.2022.07.003.

Miao, L., Wang, F., Han, J. & Lv, W. (2014). Benefits of geosynthetic reinforcement in widening of embankments subjected to foundation differential settlement. *Geosynthetics International*, **21**, No. 5, 321–332.

Nguyen, B. T. (2016). *Failure of Deep Mixing Column Group Reinforced by Shallow Mixing Layer*, PhD thesis, Tokyo Institute of Technology, Tokyo, Japan.

Nguyen, B., Takeyama, T. & Kitazume, M. (2016). Internal failure of deep mixing columns reinforced by a shallow stabilized soil beneath an embankment. *International Journal of Geosynthetics and Ground Engineering*, **2**, No. 4, 1–13.

Nie, J., Cui, Y. F., Senetakis, K., Guo, D., Wang, Y., Wang, G. D., Feng, P., He, H. Y., Zhang, X. H., Zhang, X. P., Li, C. H., Zheng, H., Hu, W., Niu, F. J., Liu, Q. X. & Li, A. Y. (2023). Predicting residual friction angle of lunar regolith based on Chang'e-5 lunar samples. *Science Bulletin*, **68**, No. 7, 730–739.

Randolph, M. F., Gourvenec, S. & Acosta-Martinez, H. E. (2009). Experimental study of uplift resistance of shallow skirted foundations in clay under transient and sustained concentric loading. *Géotechnique*, **59**, No. 6, 525–537.

Rowe, R. K. & Soderman, K. L. (1985). An approximate method for estimating the stability of geotextile-reinforced embankments. *Canadian Geotechnical Journal*, **22**, No. 3, 392–398.

Rowe, R. K. & Soderman, K. L. (1987). Stabilization of very soft soils using high strength geosynthetics: the role of finite element analyses. *Geotextiles and Geomembranes*, **6**, No. 1–3, 53–80.

Schofield, A. N. (1980). Cambridge geotechnical centrifuge operations. *Géotechnique*, **30**, No. 3, 227–268.

Sharma, J. S. & Bolton, M. D. (1996). Centrifuge modelling of an embankment on soft clay reinforced with a geogrid. *Geotextiles and Geomembranes*, **14**, No. 1, 1–17.

Shen, P., Xu, C. & Han, J. (2020). Centrifuge tests to investigate global performance of geosynthetic-reinforced pile-supported embankments with side slopes. *Geotextiles and Geomembranes*, **48**, No. 1, 120–127.

Thielicke, W. & Sonntag, R. (2021). Particle image velocimetry for MATLAB: accuracy and enhanced algorithms in PIVlab. *Journal of Open Research Software*, **9**, No. 1, 12, https://doi.org/10.5334/jors.334.

UIC (Union Internationale Des Chemins de Fer) (2018). *RAILISA. Rail transport in the world*. See https://uic.org/support-activities/statistics/#Railisa (accessed 31.08.23).

Villalobos Jara, F. A. (2006). *Model Testing of Foundations for Offshore Wind Turbines*, PhD thesis, University of Oxford, Oxford, UK.

Viswanadham, B. V. S. & König, D. (2009). Centrifuge modeling of geotextile-reinforced slopes subjected to differential settlements. *Geotextiles and Geomembranes*, **27**, No. 2, 77–88.

Wang, L., Zhang, G. & Zhang, J. M. (2011). Centrifuge model tests of geotextile-reinforced soil embankments during an earthquake. *Geotextiles and Geomembranes*, **29**, No. 3, 222–232.

Wang, L. Z., Wang, H., Zhu, B. & Hong, Y. (2018). Comparison of monotonic and cyclic lateral response between monopod and tripod bucket foundations in medium dense sand. *Ocean Engineering*, **155**, 88–105.

Wang, X., Cheng, C., Li, J., Zhang, J., Ma, G. & Jin, J. (2023). Automated monitoring and evaluation of highway subgrade compaction quality using artificial neural networks. *Automation in Construction*, **145**, 104663.

Yang, S., Leshchinsky, B., Cui, K., Zhang, F. & Gao, Y. (2019). Unified approach toward evaluating bearing capacity of shallow foundations near slopes. *Journal of Geotechnical and Geoenvironmental Engineering*, **145**, No. 12, 04019110.

Ye, G. B., Wang, M., Zhang, Z., Han, J. & Xu, C. (2020). Geosynthetic-reinforced pile-supported embankments with caps in a triangular pattern over soft clay. *Geotextiles and Geomembranes*, **48**, No. 1, 52–61.

Yodsomjai, W., Keawsawasvong, S. & Lai, V. Q. (2021). Limit analysis solutions for bearing capacity of ring foundations on rocks using Hoek–Brown failure criterion. *International Journal of Geosynthetics and Ground Engineering*, **7**, No. 2, 29.

Yuan, R., Yu, H. S., Hu, N. & He, Y. (2018). Non-coaxial soil model with an anisotropic yield criterion and its application to the analysis of strip footing problems. *Computers and Geotechnics*, **99**, 80–92.

Zhang, L. (1999). Settlement patterns of soft soil foundations under embankments. *Canadian Geotechnical Journal*, **36**, No. 4, 774–781.

Zhang, G. & Wang, L. (2010). Stability analysis of strain-softening slope reinforced with stabilizing piles. *Journal of Geotechnical and Geoenvironmental Engineering*, **136**, No. 11, 1578–1582.

Zhang, G., Hu, Y. & Wang, L. (2015). Behaviour and mechanism of failure process of soil slopes. *Environmental Earth Sciences*, **73**, No. 4, 1701–1713.

Zhang, G., Wang, L. & Wang, Y. (2017). Pile reinforcement mechanism of soil slopes. *Acta Geotechnica*, **12**, No. 5, 1035–1046.

Zhang, X., Rajesh, S., Chen, J. F. & Wang, J. Q. (2021). Geosynthetic encased column-supported embankment: behavior with and without basal geogrid. *Geosynthetics International*, **29**, No. 3, 312–325.

Zheng, G., He, X. & Zhou, H. (2023a). A prediction model for the deformation of an embedded cantilever retaining wall in sand. *International Journal of Geomechanics*, **23**, No. 3, 06023001.

Zheng, G., Xia, B., Zhou, H., Yu, X. & Diao, Y. (2023b). Influence of deep-cement-mixing column rows on the performance of geosynthetics-reinforced column-supported railway embankment. *Transportation Geotechnics*, **41**, 101012.

Zhou, H., Zheng, G., Liu, J., Yu, X., Yang, X. & Zhang, T. (2019). Performance of embankments with rigid columns embedded in an inclined underlying stratum: centrifuge and numerical modelling. *Acta Geotechnica*, **14**, No. 5, 1571–1584.

Zhou, H., Liu, X., Tan, J., Zhao, J. & Zheng, G. (2023a). Seismic fragility evaluation of embankments on liquefiable soils and remedial countermeasures. *Soil Dynamics and Earthquake Engineering*, **164**, 107631.

Zhou, H., Shi, Y., Yu, X., Xu, H., Zheng, G., Yang, S. & He, Y. (2023b). Failure mechanism and bearing capacity of rigid footings placed on top of cohesive soil slopes in spatially random soil. *International Journal of Geomechanics*, **23**, No. 8, 04023110.

Zhu, H. H., Wang, Z. Y., Shi, B. & Wong, J. K. W. (2016). Feasibility study of strain-based stability evaluation of locally loaded slopes: insights from physical and numerical modeling. *Engineering Geology*, **208**, 39–50.

The Editor welcomes discussion on all papers published in Geosynthetics International. Please email your contribution to discussion@geosynthetics-international.com by 15 April 2025